Journal of
Marine Science and Engineering

MDPI

Article

Computational Study on Influence Factors and Vortical Structures in Static Drift Tests

Chen Yang [1,*], Ke Zeng [1], Jilong Chu [1], Shuxia Bu [1,2] and Zhang Zhu [1]

[1] China Ship Scientific Research Center, Wuxi 214082, China; cssrc702zk@163.com (K.Z.); long8616767@163.com (J.C.); bushuxia@cssrc.com.cn (S.B.); zhuzhang@cssrc.com.cn (Z.Z.)
[2] Taihu Laboratory of Deep-Sea Technological Science, Wuxi 214082, China
* Correspondence: yangchen@cssrc.com.cn

Abstract: This paper conducted a computational study on the KCS benchmark model at static drift conditions. At the first instance, the roles played by the grid size, turbulence model, and time step are qualitatively and quantitatively analyzed with the orthogonal experimental method (OEM). After the verification of simulated results compared with experimental data in a Static Oblique Towing Test (OTT), hydrodynamic performance is obtained with the employment of the SST κ-ω turbulence model. The grid size is set as 0.07 m while the time step as 0.01 s. The characteristics of the wake field are illustrated in different forms, such as contours of the free surface, distribution of pressure and hydrodynamic forces, variation of turbulent kinetic energy (TKE), and so on. For a deep insight into the physical mechanisms of the asymmetrical flow field, the Detached Eddy Simulation (DES) method is also utilized to capture vortical structures occurring around the hull, in comparison with results obtained through the Reynolds Averaged Navier Stokes (RANS) model. With the aim of a hydrodynamic derivative estimation or detailed flow characteristics analysis, corresponding selections of the computational method are disparate.

Keywords: static oblique towing test (OTT); CFD; turbulence model; vortical structure

Citation: Yang, C.; Zeng, K.; Chu, J.; Bu, S.; Zhu, Z. Computational Study on Influence Factors and Vortical Structures in Static Drift Tests. *J. Mar. Sci. Eng.* **2024**, *12*, 789. https://doi.org/10.3390/jmse12050789

Academic Editor: Manhar R. Dhanak

Received: 17 April 2024
Revised: 3 May 2024
Accepted: 6 May 2024
Published: 8 May 2024

1. Introduction

Identified as a significant factor for navigational safety, an accurate prediction of ship maneuverability is of great necessity [1]. Experimental measurements are usually carried out for the estimation of hydrodynamic derivatives, and serve as input of mathematical models to predict ship motion, which is in demand of expenditure, labor, and experience [2,3]. The determination of hydrodynamic derivatives is fundamental for the establishment of a model. Taking both rotational and viscous effects of fluid into consideration [4], compared with simplified potential flow theory, Computational Fluid Dynamics (CFD) methods have the advantage in the description of the viscous effect of fluid, resulting in higher accuracy in predicting. No matter a full scale or model scale [5], CFD methods show great promise to work as a substitute for experimental approaches [6].

Compared to results from experimental measurements and potential flow computations, there is a better agreement in the ship response between results from the URANS codes CFDSHIP-IOWA and experimental measurements, especially in calm water. Carrica et al. [7] utilized the advanced version of CFDSHIP-IOWA V4.5 to calculate ship motions in head waves for a model-scaled KCS with a rudder in close proximity to the propeller. The wake field close to the vessel is obtained through the DES turbulence approach. Due to the lack of an appropriate maneuvering basin with a current generator, as well as relevant control units and measurement devices, there are few studies focused on free-running model tests in currents. Instead of highly laborious experiments, Kim et al. [8] deployed a CFD method with high fidelity to analyze the effect of currents on ship maneuverability.

After decades of development in computer technology, direct CFD simulation [9] has undisputed competence in reproducing a flow field, especially details. Owing to tremendous technological progress, researchers have conducted virtual maneuvering model tests for ships by solving equations of motion for fluid and rigid bodies. To save computational resources, RANS equations [10] are widely used instead of direct solving methods, in modeling viscous turbulent flow. Large amounts of successful cases involved S175 [11], DTMB 5415 [12], KVLCC2 [13], KRISO Container Ship (KCS) [14], and so on.

Zhang et al. [15] applied the viscous method to predict the roll motion of KCS in calm water and then converted it to equivalent linearized roll damping. Subsequently, the occurrence of parametric rolling in regular head waves could be achieved. Yu et al. [16] selected one discretized propeller model (DPM) for simulating the turning circle test at a rudder angle of 35° under the condition of Fr = 0.26. Three body force models [17–19] were also applied and an analysis was made on ship turning circles. Based on results derived from four propulsion models, differences are noticeable with a drift angle exceeding 10°. Simonsen et al. [20] carried out a study by the CFD method to calculate the added resistance and motions of a ship with an appendage in regular head seas. Served as a cost-effective method for obtaining self-propulsion factors, Can et al. [21] applied a CFD method in combination with Telfer's GEOSIM method to investigate the effective wave factor. Three model scales, as well as the full-scale condition, were investigated, and an accurate effective wake fraction of the full-scaled KCS was extrapolated.

Despite the prediction of the combined seakeeping and maneuvering performance, Kim et al. [22] introduced a CFD approach that could be used to study the course-keeping ability of the KCS. Simultaneously, the effect of wave directions on turning maneuvers could also be investigated. Generally speaking, the application of CFD methods to maneuvering is less mature compared to the solution of resistance [23]. The existence of an unsteady flow, ship motion, and variable environment increases the complexity of numerical simulation [24]. Yuan [25] found that the asymmetric flow passing on two sides of a hull results in a lifting force, which contributes to the yaw moment.

A suitable pattern of computational settings for virtual static captive model tests has not been established in the existing literature due to limited research efforts. In this work, great emphasis is placed on a systematic analysis concerning the OTT. An orthogonal experimental method (OEM) is applied to discuss the effects of different influence factors, including the turbulence model, grid size, and time step. Additionally, an uncertainty analysis was performed during the calculation of hydrodynamic forces and moment, with the adoption of the Grid Convergence Index (GCI) method. On this basis, a satisfactory computational setup for a virtual oblique towing test is achieved, and simulations are conducted at drift angles ranging from 0° to 12°. In addition to non-uniform force distribution and free surface elevation, vortical structures are captured to provide a comprehensive understanding of the asymmetric flow field. This work contributes to advancing the numerical solutions for virtual static captive model tests.

2. Numerical Method

2.1. Governing Equations

In this study, the commercial software STAR-CCM+ 16.06 is utilized for the simulation of three-dimensional viscous flow around the hull. Taking calculating resource and computing time into account, this work applied RANS equations instead of solving NS equations directly, which include Reynolds stress terms characterizing the turbulence effect. Under the assumption of impressible flow, relevant equations for the description of two-phase turbulent flow can be presented as follows:

$$\frac{\partial(\varphi_m \rho_m)}{\partial t} + \frac{\partial}{\partial x_i}(\varphi_m \rho_m \overline{u_i}) = 0 \quad (1)$$

$$\frac{\partial \rho_m \overline{u_i}}{\partial t} + \frac{\partial}{\partial x_j}\left(\rho_m \overline{u_i u_j}\right) = -\frac{\partial \overline{P}}{\partial x_i} + \frac{\partial}{\partial x_j}\left[\mu_m\left(\frac{\partial \overline{u_i}}{\partial x_j} + \frac{\partial \overline{u_j}}{\partial x_i}\right)\right] + \frac{\partial}{\partial x_j}\left(-\rho_m \overline{u_i{}' u_j{}'}\right) + \rho_m \overline{f_i} \quad (2)$$

where m represents the phase id concerning water and air; i and j are coordinate components of velocity; u denotes velocity; ρ stands for density; μ is viscosity; P means pressure; f refers to gravity in this work; and $\overline{u_i{}' u_j{}'}$ indicates the Reynolds stress term based on the Boussinesq hypothesis, and a specific explanation can be found in reference [4].

2.2. Ship Geometry

The well-known benchmarking KCS is studied for simulation at a scale factor of 1/75.5. It is worth mentioning that a fixed rudder is located at the stern of the ship model, at a distance of nearly three meters from the bow, as displayed in Figure 1. Principal characteristics of the ship geometry are obtained from SIMMAN (2014) [26] and listed in Table 1. For the sake of a validation analysis, experimental results were released by the National Maritime Research Institute (NMRI).

Figure 1. The side view of the KCS model.

Table 1. Dimensions of KCS including the full scale and model scale.

Description	Parameter	Unit	Full Scale	Model Scale
Length between perpendiculars	L_{pp}	m	230	3.046
Beam at waterline	B_{wl}	m	32.2	0.427
Draught	T	m	10.8	0.143
Volume of displacement	∇	m^3	52,030	0.121
Block coefficient	C_B	-	0.651	0.651
Wetted surface area	S	m^2	9530	1.688
Metacentric height	GM	m	0.600	0.097

2.3. Case Description of Simulation

From Figure 2, a Cartesian coordinate system is fixed on the ship, with positive x, y, and z axes pointing to the upstream, portside, and upward directions in sequence. The origin is set as the intersection of the central longitudinal section, the midship section, and the water plane, and the vessel is upright without any trim at the beginning. The length of the computational domain starts from 2.7 L_{pp} to 4.0 L_{pp} in the longitudinal direction, while the width from 3.2 L_{pp} to 2.5 L_{pp} in the horizontal direction due to the symmetrical incoming flow. The construction of the virtual tank in the height direction is defined as consistent with the depth of the maneuvering basin in the NMRI. The setup of boundary conditions is summarized in Table 2, including the velocity inlet, the pressure outlet, and no-slip walls. To eliminate the effect of boundaries, a wave damping zone is specified near the rear part of the virtual tank.

Table 2. Summary of boundary conditions involved in this work.

Name of Boundary	Type of Boundary Condition
Inlet	Velocity inlet
Outlet	Pressure outlet
Side_R	Velocity inlet
Side_L	Velocity inlet
Top	Velocity inlet
Bottom	Velocity inlet
Hull surface	No-slip wall

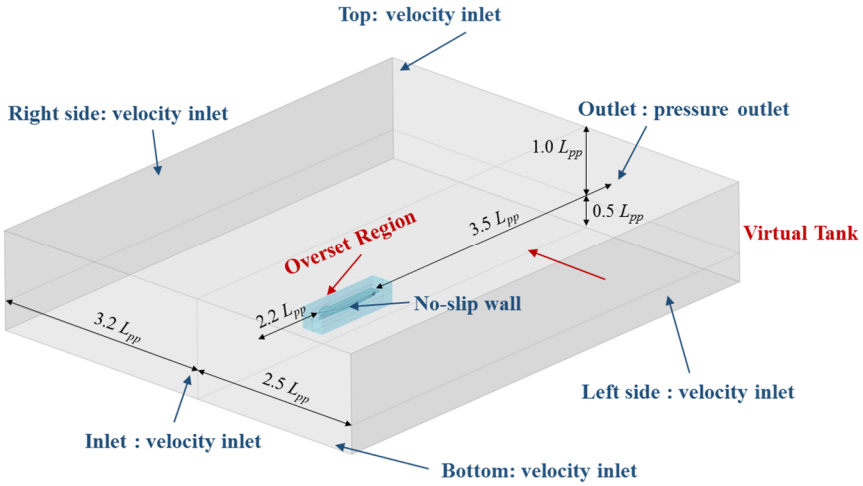

Figure 2. The setup of the computational domain.

Figure 3 displays the mesh structure of simulation. The trimmed mesher and the surface remesher are applied for mesh discretization. The latter is employed to generate volume meshes, while the former is used for surface meshes. Specifically, the prism mesh was generated at the boundary layer close to hull surfaces, with a layer number of six. To satisfy the requirement of $30 < y+ < 100$, the total thickness of the boundary layer is limited to 0.042 m. For a reasonable mesh distribution instead of a uniform grid, three refinement levels are identified from inside out. The interface of the two-phase flow is another refinement region to capture the elevation in the free surface precisely. Additionally, the VOF method, one of the multiphase flow models, is adopted to identify phases of water and air. Taking the complexity of specific geometric structures into consideration, local mesh refinement is also implemented in parts including the bow, the stern, and the rudder. A three-degree-of freedom vessel is investigated by solving the equations for rigid body motion, including heave, pitch, and roll motions during the simulation.

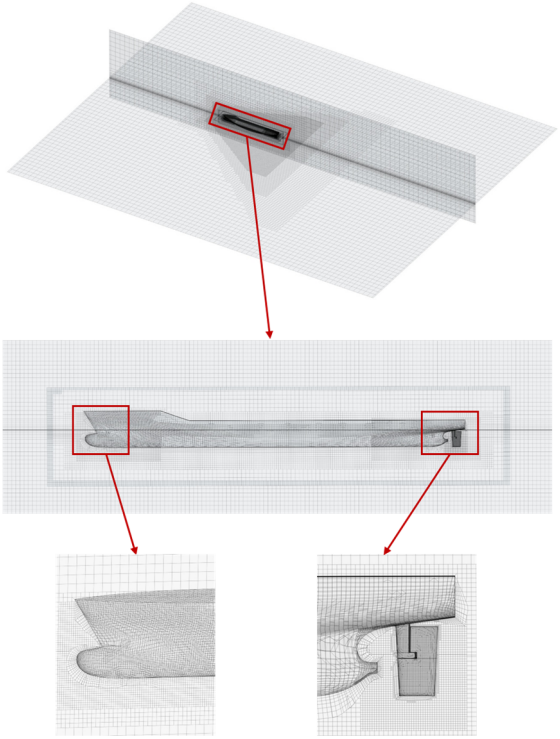

Figure 3. Mesh structure of simulation.

Virtual oblique towing tests contain conditions of drift angles ranging from 0° to 12°. Table 3 introduces specific working conditions of simulation. The velocity v_m of the ship model is constant, corresponding to a Froude number (Fr) of 0.20.

Table 3. Computational case conditions.

Drift Angle (deg)	Velocity of Model (m/s)	*Fr*
0, 4, 8, 12	1.1	0.20

When conducting the simulation of the OTT, ship motions are confined to the transverse X-Y plane. Hence, particular attention is paid to longitudinal force X, lateral force Y, and yaw moment N. For simplification, non-dimensional longitudinal force X' and lateral force Y' can be derived by dividing $\frac{1}{2}\rho {v_m}^2 L_{pp} d$, while non-dimensional yaw moment $N' = \frac{N}{\frac{1}{2}\rho {v_m}^2 {L_{pp}}^2 d}$.

2.4. Orthogonal Uncertainty Analysis

During the use of numerical tools, great necessity is attached to an uncertainty analysis relating to multi-factors. When estimating numerical errors and uncertainties, at least three sets of data in relation to one variable are in demand for verification. Considering the efficiency of the analysis, the OEM is utilized for the simulation of the OTT. The application of the turbulence model is deemed as influence factor A, selection of grid base size is regarded as influence factor B, and setting of the time step is taken as influence factor C. Figure 4 illustrates the workflow of the orthogonal uncertainty analysis method employed in this work.

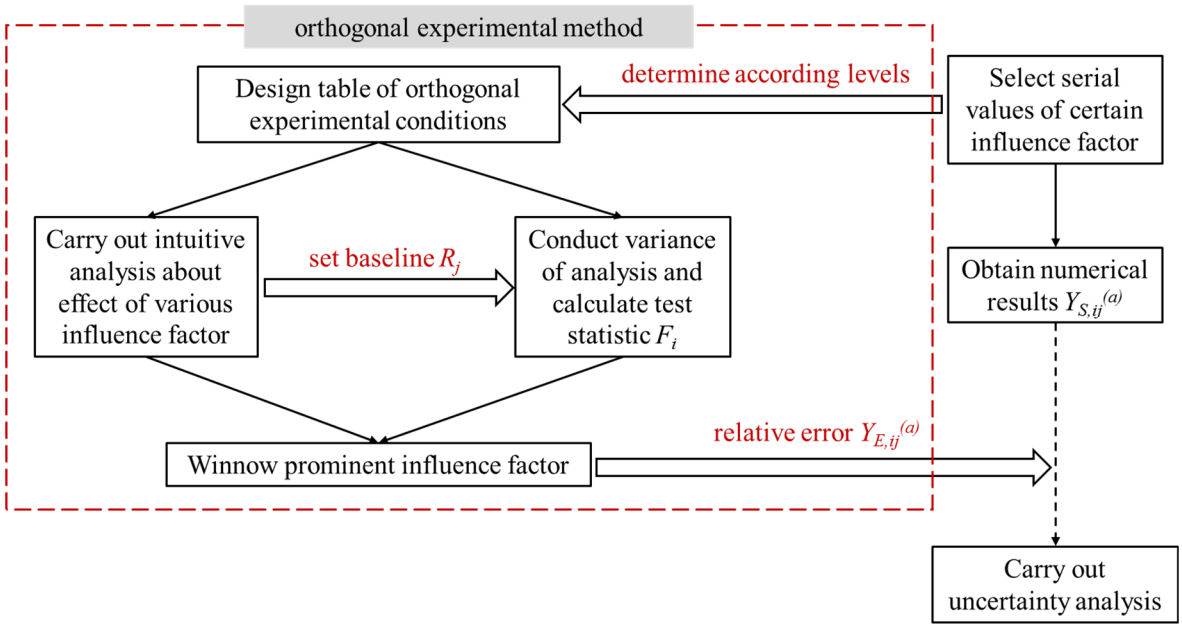

Figure 4. Workflow of orthogonal uncertainty analysis method.

During orthogonal experimental tests, the count of test conditions is denoted as n, while the number of influence factors as p and number of levels as q. For convenience, the relevant indicator of an experiment with a serial number of a is denoted by $Y_{ij}^{(a)}$, where i represents the order of the influence factor and j stands for the order of the level, respectively. Average values at targeted levels K_{ij} play a significant role in the OEM including an intuitive

analysis and variance analysis, implemented as a qualitative analysis and quantitative analysis, respectively. Calculation equations are provided as follows:

$$K_{N,ij} = \frac{q}{n}\sum_{a=1}^{n/q} Y_{N,ij}^{(a)} \tag{3}$$

$$K_{E,ij} = \frac{q}{n}\sum_{a=1}^{n/q} Y_{E,ij}^{(a)} \tag{4}$$

where subscript 'N' represents data obtained by means of numerical simulation and 'E' refers to the relative error between results calculated from the numerical method and experimental measurement. To put it another way, ${K_{N,ij}}^{(a)}$ stands for numerical results of influence factor i at the level j (denoted as serial number of a). In this work, ${Y_{N,ij}}^{(a)}$ is deployed in the uncertainty analysis and ${Y_{E,ij}}^{(a)}$ is calculated for comparison between influence factors.

In a gesture to the winnow prominent influence factor, which has a great impact on the relative error, an analysis of variance is conducted alongside the intuitive analysis. The definition of extreme deviation R_j is shown as Equation (6), and the influence factor corresponding to the minimum value of extreme deviation will be taken as the baseline:

$$R_j = \max\left(K_{E,ij}\right) - \min\left(K_{E,ij}\right) \tag{5}$$

Take the relative error of influence factor i at the level j (denoted as serial number of a) ${Y_{E,ij}}^{(a)}$ as an indicator, and the average of results is as follows:

$$\overline{T} = \frac{1}{n}\sum Y_{E,ij}^{(a)} \tag{6}$$

Then, S_i stands for the sum of the standard deviation, which is concerned with all influence factors:

$$S_i = \frac{n}{q}\sum_{j=1}^{q}\left(K_{E,ij} - \overline{T}\right)^2 \tag{7}$$

After the summation of standard deviation obtained through Equation (7), mean square MS_i can be calculated as follows:

$$MS_i = S_i/f_i = \frac{n}{q}\sum_{i=1}^{q}\left(K_{E,ij} - \overline{T}\right)^2 \Big/ (p-1) \tag{8}$$

where f_i indicates the degree of freedom.

Aiming at quantifying the effect of the influence factor, test statistic F_i is applied to compare impact with the baseline, which is written as follows:

$$F_i = S_i/S_e \tag{9}$$

where S_e corresponds to the sum of the standard deviation for the influence factor with the minimum extreme deviation.

A smaller value of the test statistic indicates a less significant role. Hence, influence factors with a test statistic below the reference value will not be taken into account in the subsequent uncertainty analysis. For space reasons, relevant procedures will not be introduced in this paper, which can be found in published study [27].

3. Numerical Results

3.1. Effect of Selected Influence Factors

During the simulation of an OTT, an OEM is utilized for a comprehensive analysis on the effects of various computational settings. Definitions of influence factors *A*, *B*, and *C* are stated in Section 2.4. For each influence factor, three different levels are chosen for the analysis, as presented in Table 4. With regard to the turbulence model, level 1 and 2 stand for the widely used two-equation models SST κ-ω model and Realizable κ-ε model, respectively. A Reynolds Stress Model (RSM) is represented by level 3, which is another effective tool to address complex flow phenomena. Taking the grid discretization method and computing time into account, the DES model or LES model is excluded from the design of an orthogonal array. Concerning grid convergence research, a refinement ratio of $\sqrt{2}$ is chosen according to reference [27] in maneuvering tasks.

Table 4. Relative error of test conditions by OEM.

No.	Influence Factor A	Influence Factor B	Influence Factor C	State of Conditions	Relative Error (%)
1	SST κ-ω	0.05 m	5×10^{-3} s	$A_1B_1C_1$	−12.54
2	SST κ-ω	0.07 m	0.01 s	$A_1B_2C_2$	−10.81
3	SST κ-ω	0.10 m	0.02 s	$A_1B_3C_3$	−6.74
4	Realizable κ-ε	0.05 m	0.01 s	$A_2B_1C_2$	−12.43
5	Realizable κ-ε	0.07 m	0.02 s	$A_2B_2C_3$	−9.64
6	Realizable κ-ε	0.10 m	5×10^{-3} s	$A_2B_3C_1$	−6.02
7	RST	0.05 m	0.02 s	$A_3B_1C_3$	−10.45
8	RST	0.07 m	5×10^{-3} s	$A_3B_2C_1$	−7.82
9	RST	0.10 m	0.01 s	$A_3B_3C_2$	−1.72

The orthogonal array is also illustrated in Table 4 as the column of 'State of Conditions', indicating the parameter configuration for the numerical simulation. Two principles for the design of test conditions are the uniform distribution and homogeneous design. To guarantee the orthogonality of the test design, the occurrence frequencies of level 1, 2, and 3 for the influence factor are identical. In addition to this, the combination of level orders concerning either of the two influence factors is also the same. Values of relative errors related to each state of experimental conditions are also provided. Among all conditions, it can be observed that data obtained through the CFD method are smaller than experimental results. The peak value of the relative error comes to −12.54% under the experimental condition of $A_1B_1C_1$, while the minimum value is about −1.72%.

Average values at different levels are listed in Table 5, together with extreme deviations of three influence factors, which reflect the extent of significance. From the results, the impact exerted by the influence factor *C* is negligible. With the variation of the time step from 0.01 s to 0.02 s, the extreme deviation is only 0.62%. As a result, the time step is chosen as the baseline factor for the variance analysis. Values of the test statistic are consistent with the extent of significance obtained from extreme deviation. The impact of grid base size imposed on the numerical results cannot be ignored. Compared with the time step, the test statistic of grid size reaches 32.32, which is larger than the reference value of $F_{0.95} = 19$. Among the three influence factors, grid size plays the most significant role in numerical simulation, followed by the turbulence model.

In order to carry out an intuitive comparison of results obtained with different turbulence models, the longitudinal force and lateral force are plotted under an *Fr* of 0.20 as displayed in Figure 5. During post-processing, the ship hull is divided into 100 parts at an interval of $\Delta x/L_{pp} = 0.01$. Values of each part can be obtained by means of integration according to the active area. The force induced by pressure and viscous effect are designated as subscripts *p* and *s*, respectively. For instance, physical quantity X_p represents the part of longitudinal force deriving from pressure while Y_s denotes the part of lateral force resulting from friction. The drift angle is chosen as 12° for a more conspicuous separate flow in the

virtual test. In the figure, the ordinate represents the variation in the longitudinal direction with a non-dimensional parameter x/L_{pp} for convenience, while the abscissa represents the values of forces. From the gradient of value, the pressure component makes a major contribution, particularly in lateral force. The grey line indicates data related to the SST κ-ω model, while the red line and blue line correspond to level 2 and level 3 of turbulence models, respectively. The diversity of the turbulence model can be observed facilely in forces stemming from the viscous effect of water, especially in the range of x/L_{pp} = 0.45~0.70. To put it another way, the discrepancy between curves of the pressure component in different colors is not as distinct as that of the shear component, which is consistent with results in Table 5.

Table 5. Intuitive analysis results and variance analysis of non-dimensional sway force Y'.

	Influence Factor *A*	**Influence Factor *B***	**Influence Factor *C***	
$K_{E,i1}$	−10.03%	−11.81%	−8.79%	
$K_{E,i2}$	−9.36%	−9.42%	−8.32%	
$K_{E,i3}$	−6.67%	−4.83%	−8.94%	
R_i	3.36%	6.98%	0.62%	
Extent of significance		B > A > C (influence factor B ranks first)		
Sum of standard deviation S_i	1.905×10^{-3}	7.550×10^{-3}	0.064×10^{-3}	
Degree of freedom f_i	2	2	2	$F_{0.95}(2,8) = 19$ $F_{0.99}(2,8) = 99$
Mean square MS_i	0.952×10^{-3}	3.775×10^{-3}	0.032×10^{-3}	
Test statistic F_i	8.154	32.32	0.272	

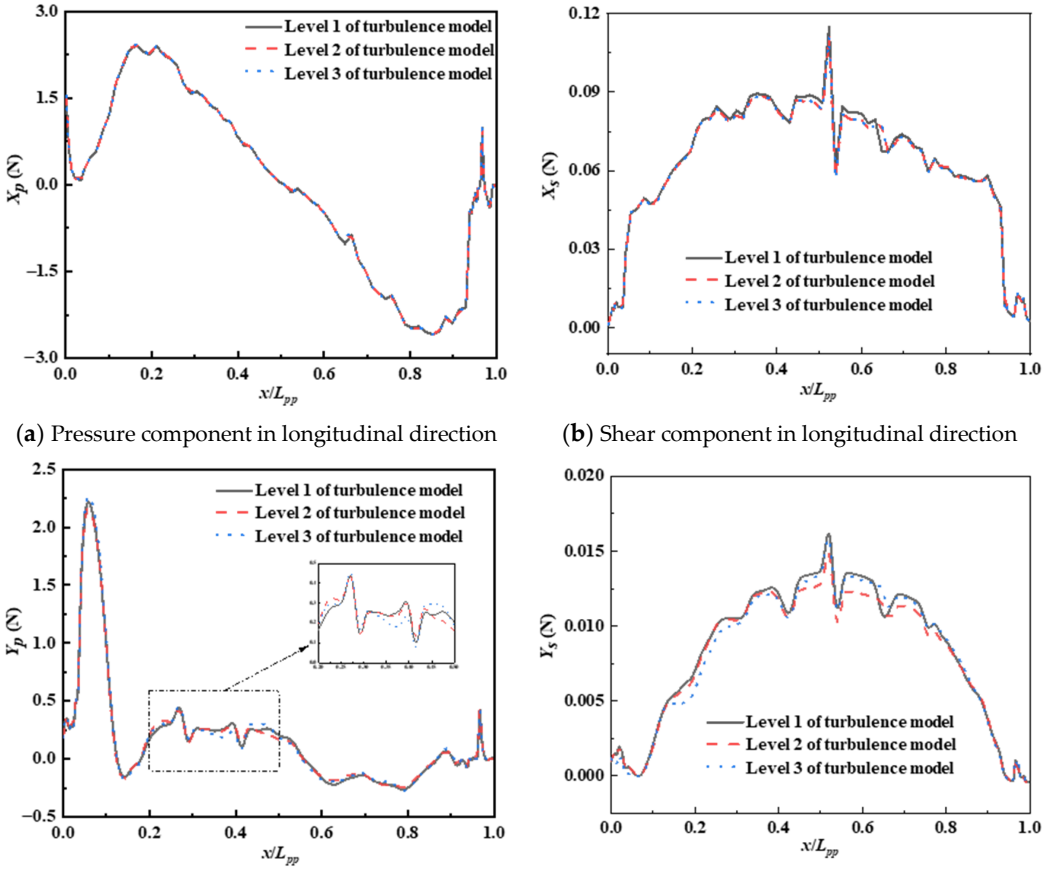

(**a**) Pressure component in longitudinal direction

(**b**) Shear component in longitudinal direction

(**c**) Pressure component in transverse direction

(**d**) Shear component in transverse direction

Figure 5. The distribution of forces along the longitudinal and the transverse directions by using different turbulence models.

To implement the requisite quantitative analysis, the GCI is applied to estimate the uncertainty caused by the grid size, which is a quantifiable influence factor. It is worth mentioning that the average value at different levels of $K_{S,ij}$ is taken as a substitute for numerical results in the grid convergence study, which can be found in Table 6. Utilizing the SST κ-ω model at a time step of 0.01 s, it only takes the influence exerted by grid size into consideration. Surge force is opposite to the forward direction, manifested as negative values in the table. For the sake of convenience, number 1 represents the fine grid, while numbers 2 and 3 stand for medium and coarse grids, respectively. Corresponding grid numbers are 4.15×10^6, 1.64×10^6, and 0.66×10^6 in sequence. To guarantee a monotonic convergence condition, hydrodynamic forces and moment are non-dimensionalized to fall in the range of 0 to 1, including dimensionless forms of drag force X', transverse force Y', and yaw moment N'. When comparing the results of adjacent convergence models with symbols 1 and 2, the approximate relative error ${e_a}^{21}$ is below the acceptable upper limit of 5%, as well as the GCI_{21} index.

Table 6. Results of grid convergence analysis.

Parameter	Dimensionless Surge Force X'	Dimensionless Sway Force Y'	Dimensionless Yaw Moment N'
$K_{S,1}$ ($\times 10^{-3}$)	−20.246	60.802	27.925
$K_{S,2}$ ($\times 10^{-3}$)	−20.260	62.447	28.157
$K_{S,3}$ ($\times 10^{-3}$)	−20.658	65.614	28.621
ε_{21}	-1.420×10^{-5}	1.6453×10^{-3}	2.319×10^{-4}
ε_{32}	-3.978×10^{-4}	3.1664×10^{-3}	4.635×10^{-4}
R	0.0357	0.5196	0.5003
p_{GCI}	3.7033	0.7524	0.7928
${e_a}^{21}$	0.070%	2.706%	0.830%
GCI_{21}	0.003%	3.332%	0.948%
${e_a}^{32}$	1.963%	5.071%	1.646%
GCI_{32}	0.091%	6.537%	1.970%

Figure 6 displays the distribution of sway force on both sides along the longitudinal direction under different grid sizes, which is also integrated by uniformly distributed sections with the same Δx. For an intuitive comparison, it has to be stressed that negative values on the portside are plotted. Under the condition of a 12° drift with v_m = 1.1 m/s, a smoother transition can be noticed with the fine grid. In other words, an increase in the grid number can bring about an improvement in accuracy to some extent. Nevertheless, when the grid number reaches a certain value, the promotion of accuracy may be negligible regarding the consumed computing resources. For convenience, we take the bow of the hull as the position of x = 0, and stern of the model as x = 1. From lateral force acting on the portside, peak values emerge at the distance of x/L_{pp} = 0.139 and 0.522, which is independent of grid size. Such a phenomenon also takes place when it comes to the starboard side, with a different peak point at x/L_{pp} = 0.064. In addition to the location of the peak value, discrepancy also exists between the magnitude of lateral force on two sides, which can be attributed to the influence of the drift angle, irrelevant to the refinement of the grid in this research. Combined with GCI values, the intermediate set of grid size, which equals 0.07 m, could satisfy the calculation accuracy of hydrodynamic force.

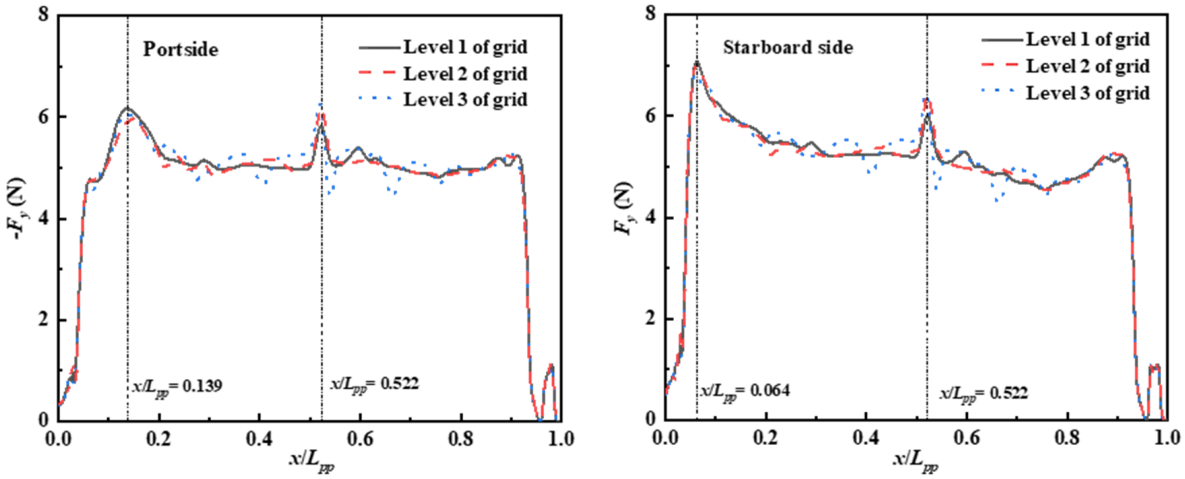

(**a**) Inverse value of lateral force at the portside (**b**) Lateral force at the starboard side

Figure 6. Lateral force at two sides under diverse grid sizes.

3.2. Numerical Results under Different Test Conditions

Based on the analysis undertaken in Section 3.1, the effects of three influence factors at various levels are investigated, and suitable computational settings for a virtual static drift test are received. The combination of both the grid size and time step at level 2, together with the RST turbulence model, is a proper selection. Apart from the simulation accuracy, the stability of the solution and the difficulty of convergence should also be considered. Hence, the SST κ-ω model is employed for simulation under several drift angles. Table 7 provides a comparison between solving results and experimental data given by the NMRI under drift angles of 6° and 12°. It can be observed that dimensionless surge force and sway force calculated through numerical simulation are smaller than those obtained by experiments, while the numerical result of the dimensionless yaw moment is larger. From the results, the maximum value of the relative error occurs when the drift angle reaches 12°, which is about 11.37% for the non-dimensional yaw moment. It can be attributed to many reasons. For a static drift test, hydrodynamic forces and moment are affected by flow separation, especially that taking place around the sonar dome. The difficulty in capturing the onset and progression increases at a larger drift angle. However, the RANS turbulence model has its limitation in shielding of the boundary layer, which may result in a large error. Additionally, the more unsteady behavior of the free surface under the condition of a 12° drift test poses a greater challenge for the grid discretization method. Inalterable grid refinement regions as the condition of small-drift-angle tests may underperform during the simulation of interaction between the fluid and ship hull. The average relative error of hydrodynamic forces and moment is nearly 10% within the acceptable range. Generally speaking, adopted computational settings can meet the requirement for the simulation of an OTT.

Table 7. Validation of the CFD method compared with experimental data provided by NMRI.

Drift Angle	Physical Quantity	Experimental Data ($\times 10^{-2}$)	Numerical Result ($\times 10^{-2}$)	Relative Error (%)
$\beta = 6°$	X'	−1.938	−1.900	−1.95
	Y'	2.338	2.220	−5.06
	N'	1.271	1.328	4.55
$\beta = 12°$	X'	−2.211	−2.072	−6.27
	Y'	6.894	6.480	−6.02
	N'	2.455	2.734	11.37

With the transformation of the drift angle, the incident direction of incoming flow alters while positioning of the vessel remains. To illustrate the interaction between the vessel and fluid, Figure 7 depicts the volume fraction of water at the bow. Under the drift angle of 0°, the distribution of water is the same on two sides of the hull. When the drift angle increases from 0° to 12°, the discrepancy between two sides can be easily observed, especially in the case of a 12° drift angle. The larger the drift angle is, the larger the difference between crests at the portside and the starboard side will be.

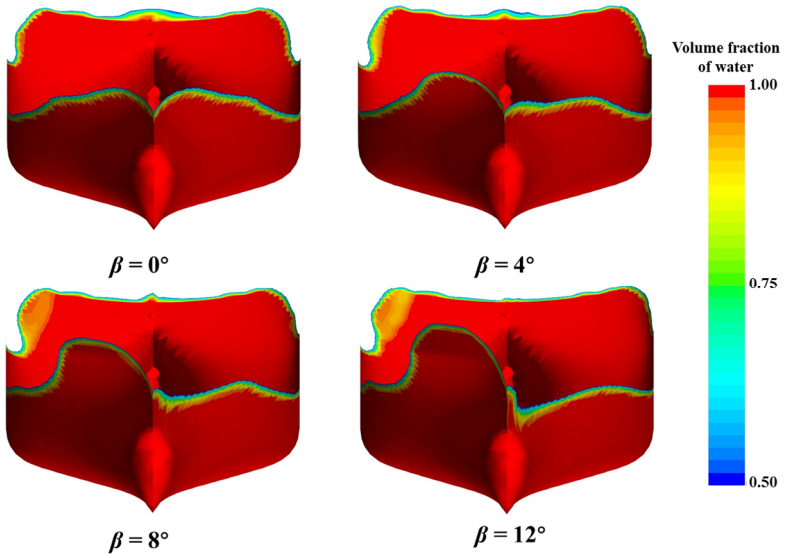

Figure 7. The general view of waterlines with a drift angle in the range of 0~12°.

For a clear representation of wave elevation, Figure 8 displays the top view of the free surface at an interval of 4° for the drift angle. The wave height at the portside and the starboard side correlates to the distribution of pressure on the hull, which is closely bound up with the acting force attributed by fluid. Apart from this, contours of the wave pattern are also displayed in Figure 8 as supplementation. The grey line denotes the portside while the red line represents the starboard side, both of which are extracted at sections located 0.072 L_{pp} away from the longitudinal section. Under different drift angles, the diversity of wave height concentrates on the region of x/L_{pp} = 0~1. In particular, critical positions can be observed near x/L_{pp} = 0.177 and x/L_{pp} = 0.828, which correspond to the regions of the fore body and the aft body, respectively. Under the 4° drift condition, the wave surface ahead of the bow is conspicuously elevated at the starboard side, with a maximum difference in wave height of 0.027 m. Accompanied by the increase in the drift angle, more obscure deviation in wave height at two sides can be observed. The dispersed waves at the portside vanish gradually with the opposite situation observed at the other side, especially in the bow region.

During the oblique towing test, the onset of the included angle between the incoming flow and the vessel will give rise to pressure differences around the hull, which can be attributed to the asymmetry of the fluid at the portside and the starboard side. It is undeniable that hydrodynamic forces and moment exerted on the vessel are deeply dependent on the flow field. From Figure 9, divergence can be observed between longitudinal distributions of pressure in drift angle tests, especially in the region of x/L_{pp} = 0~0.2. Similarly, the difference of pressure distributed at two sides is more significant with an increase in the drift angle. The existence of a bulbous bow exaggerates the difference originating from the oblique flow. After development along the longitudinal direction, there is a minor discrepancy between pressures on the two sides.

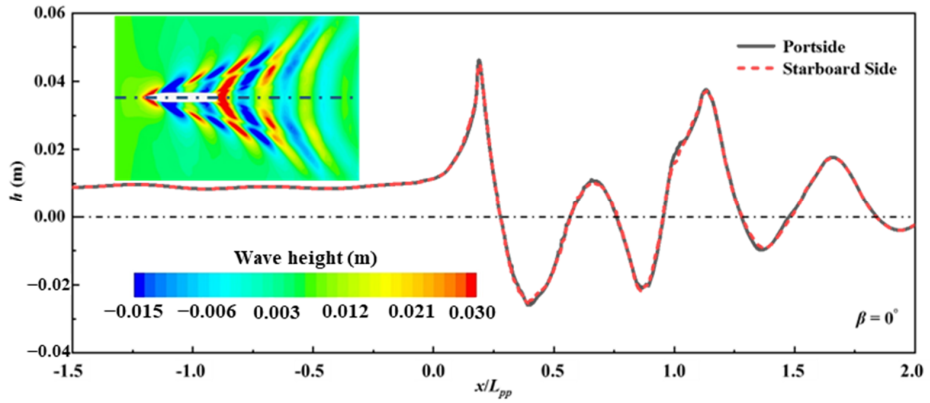

(**a**) drift angle of 0°

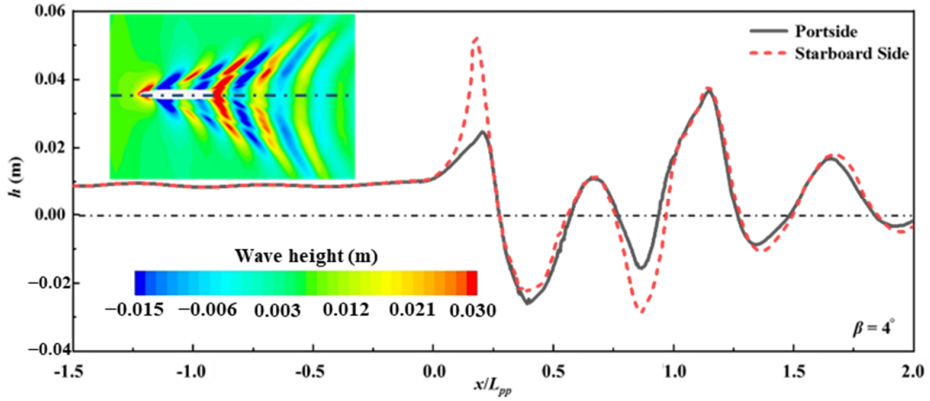

(**b**) drift angle of 4°

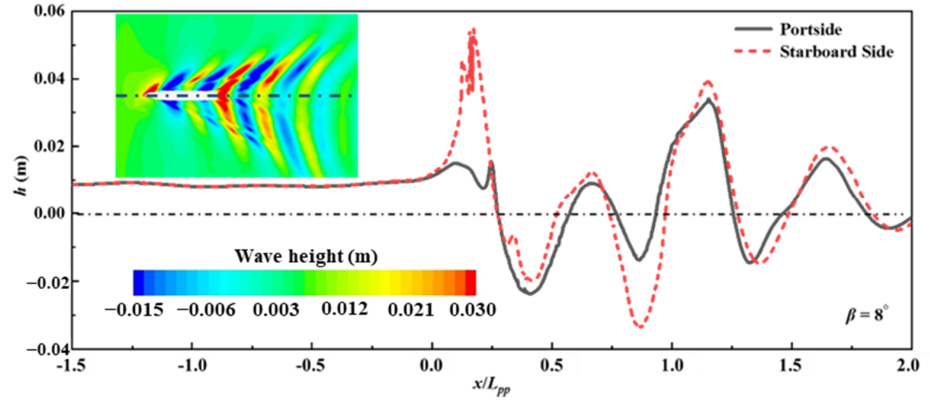

(**c**) drift angle of 8°

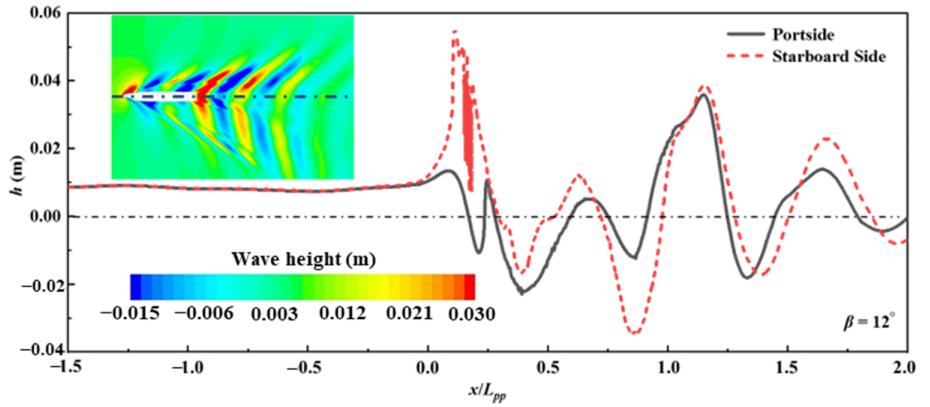

(**d**) drift angle of 12°

Figure 8. Comparison of wave height along longitudinal direction.

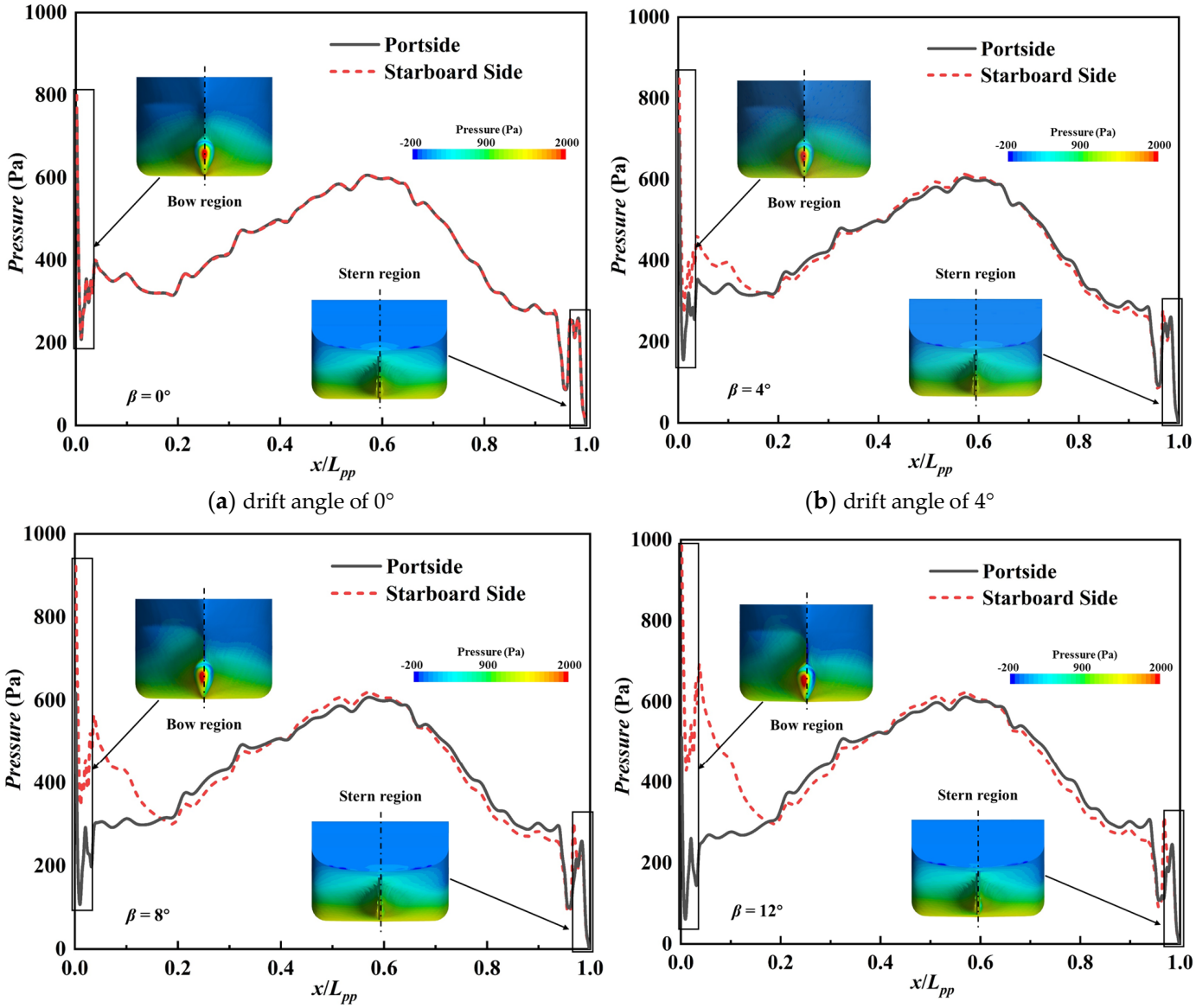

(**a**) drift angle of 0° (**b**) drift angle of 4°

(**c**) drift angle of 8° (**d**) drift angle of 12°

Figure 9. Pressure distribution on the hull along the longitudinal direction.

The pressure difference at two sides along the longitudinal section leads to disparity in the velocity component, which is a significant indicator of the flow field. The asymmetrical velocity field around the symmetrical vessel, displayed in Figure 10, results in the generation of diverse sway force, with the solid line corresponding to the portside and the dashed line for the starboard side. The distribution of fluid velocity is symmetrical under the condition of $\beta = 0°$, which is similar to Figures 7–9. It is noticeable in the difference of lateral force at two sides with an increase in the drift angle. The greatest disparity of $|F_y|$ emerges at the location of $x/L_{pp} = 0.055$ in the 12° drift angle test. At the starboard side, the maximum lateral force is 33% higher than that at the portside, which comes up to 11.94 N. For an intuitive analysis of local areas, velocity components on sections of $x/L_{pp} = 0.12$ and $x/L_{pp} = 0.88$ are also demonstrated in Figure 10, corresponding to bow and stern regions, respectively. The dimensionless parameter u' is selected for illustration, and contours are demonstrated from the perspective of the stern. The velocity component in the longitudinal direction experiences continuous reduction when the drift angle increases. In the bow region of the vessel (section $x/L_{pp} = 0.12$), fluid at the starboard side shows higher longitudinal velocity speed, especially in Figure 10d. On the contrary, the opposite appearance is

perceived at the section of x/L_{pp} = 0.88. The asymmetry in velocity component arises from the lateral flow, which brings about a leaking vortex in the region near the bulbous bow. The deviation extent of fluid will be enhanced due to the interaction between the leaking vortex and the boundary layer at the starboard side of the vessel.

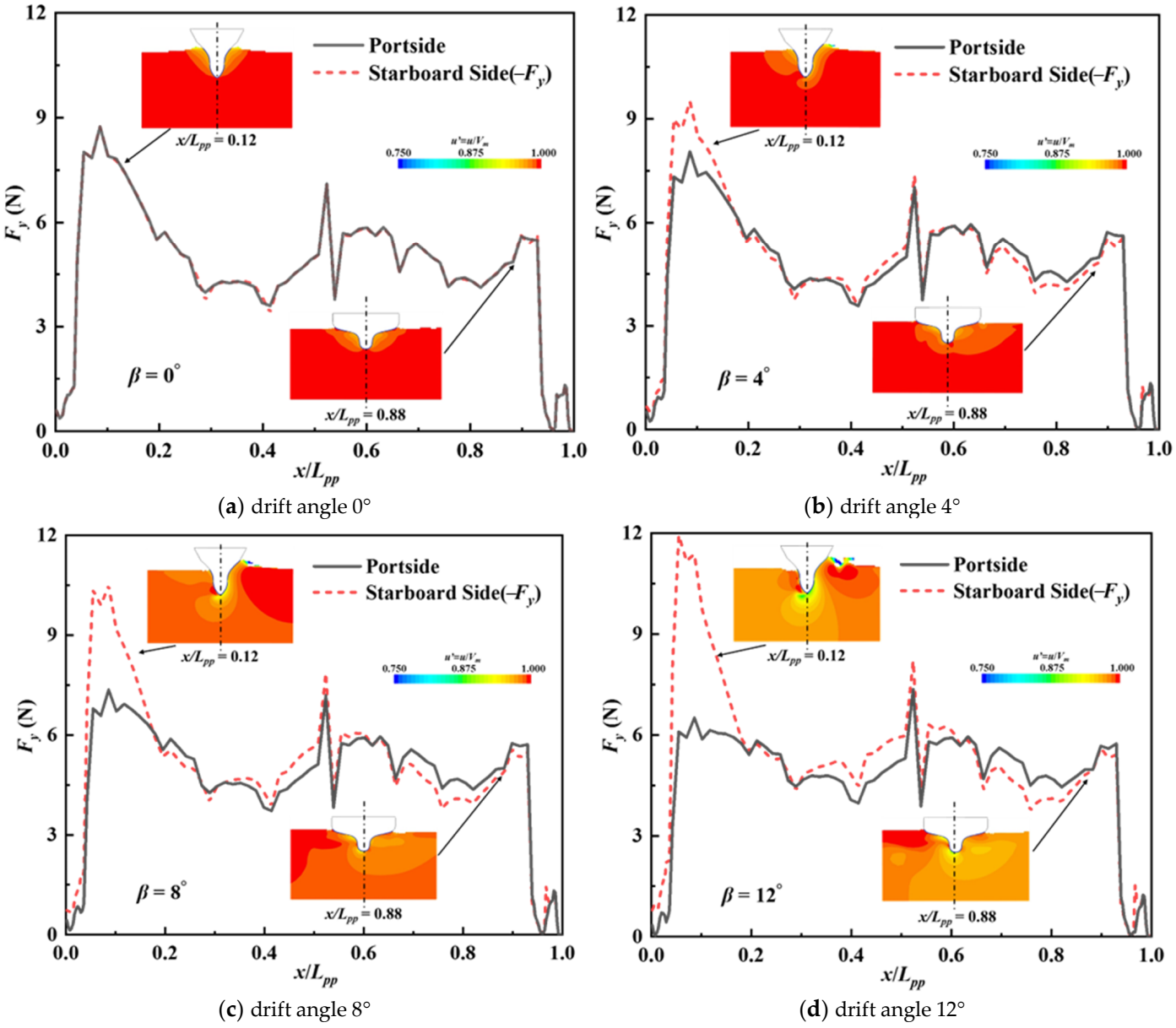

(**a**) drift angle 0° (**b**) drift angle 4°

(**c**) drift angle 8° (**d**) drift angle 12°

Figure 10. The comparison of lateral force on two sides of the hull.

The longitudinal evolution of turbulent kinetic energy is depicted in Figure 11. The asymmetry can be easily observed when the drift angle increases, which shows consistency with that of the longitudinal velocity component. Nevertheless, the magnitude is underestimated due to anisotropy in a Reynolds Stress Transport model [28]. As a result, these contours are merely appropriate for the reflection of a certain distribution pattern.

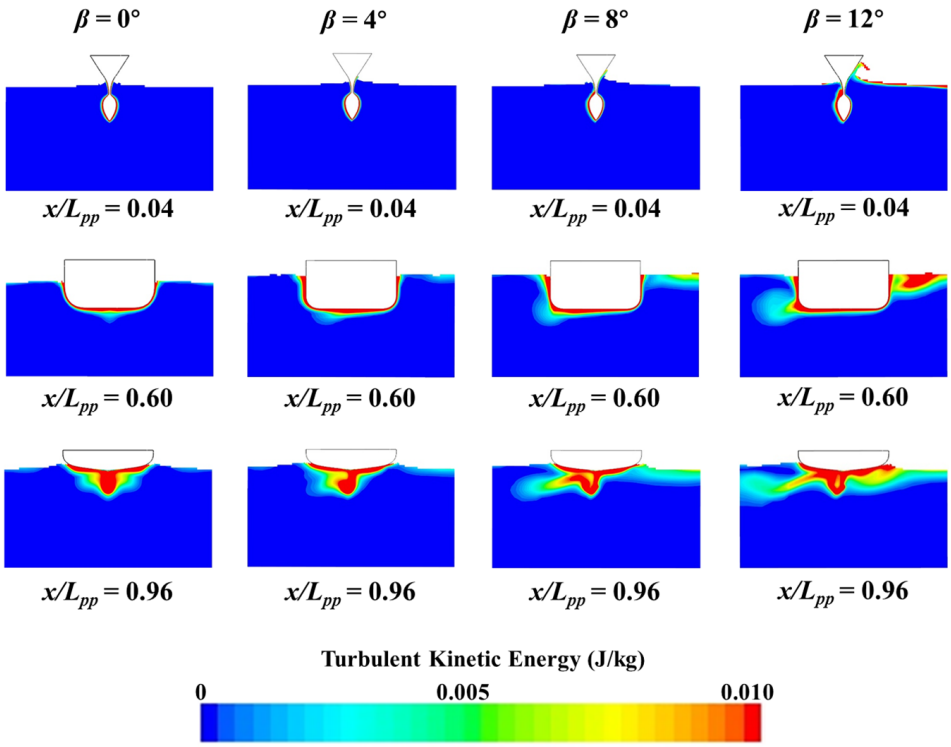

Figure 11. Turbulent kinetic energy at different sections.

3.3. Vortical Structures

With keen attention paid to detailed flow separation and realistic demand for an authentic representation of the real physics, researchers are in persistent pursuit of capturing vortex structures. In a gesture to look deeper into the physical mechanisms of the asymmetrical flow field, a comparison is made with the method of the RANS model and DES model [29]. The main time-averaged vortical structures occurring around the ship hull under a static drift condition of 12° are illustrated in Figure 12, together with the position of fluid in contrast to the free surface. For vortex identification, the iso-surface of the Q-criterion [30] is displayed with a threshold of 50, which is colored by the vorticity magnitude. The major vortex structure is the windward sonar dome tip vortex (WW-SDTV). It can be clearly distinguished from the sonar dome end tip. Under the premise of an identical grid refinement method at the same location, the discrepancy in the evolution of the WW-SDTV can be easily detected when utilizing two different models. In Figure 12b, the vortex stretches to a longer range along the hull. To put it another way, the progressive damping of the WW-SDTV simulated by the RANS method is faster. Concerning the stern vortex (SV), more detailed vortex structures are visible when utilizing the DES method. Apart from this, a smoother transition of the kelvin wave is observed, indicating a better solution over the wake field.

For the research on flow separation and vortex shedding, the development of the vortex in the direction of incoming fluid is demonstrated in Figure 13, with the extraction of six sections along the hull. From longitudinal vorticity contours, the deflection of the vortex is inconspicuous until the stern region in the 4° static drift test. Under high drift angles, the evolution of the vortex at the portside is more violent, especially for 12° DES simulation.

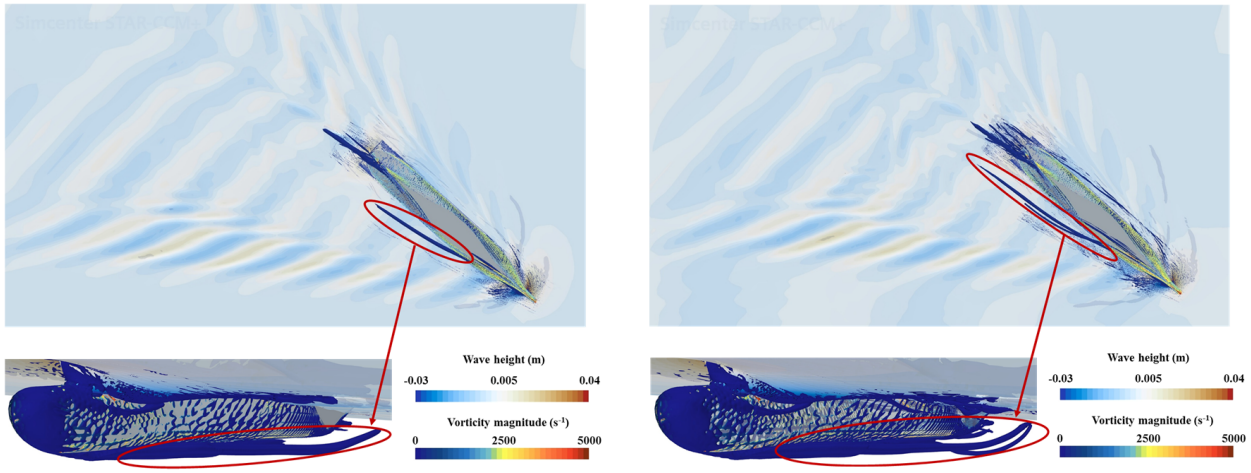

(**a**) results with the deployment of the RANS method (**b**) results with the deployment of the DES method

Figure 12. Vortex structures obtained through RANS model and DES model.

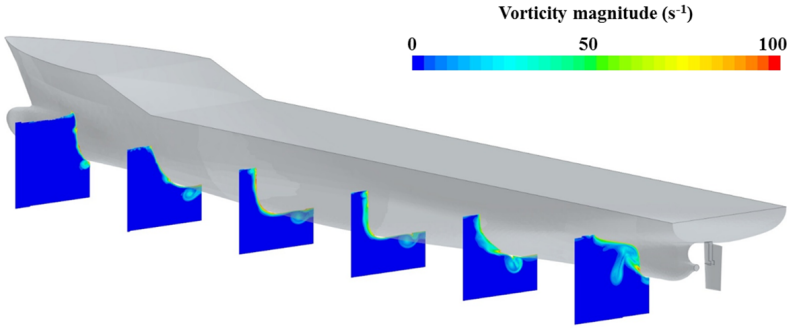

(**a**) drift angle of 4°

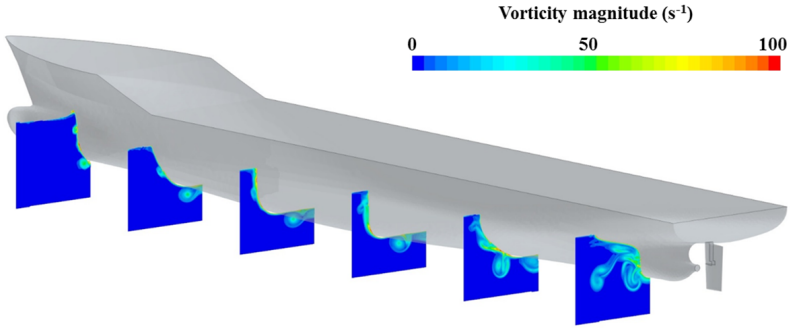

(**b**) drift angle of 6°

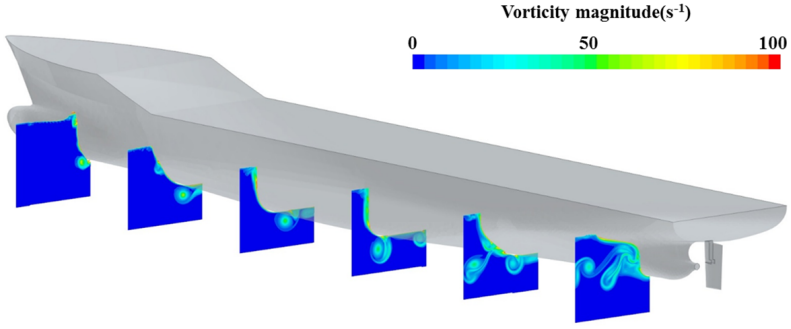

(**c**) drift angle of 8°

Figure 13. *Cont.*

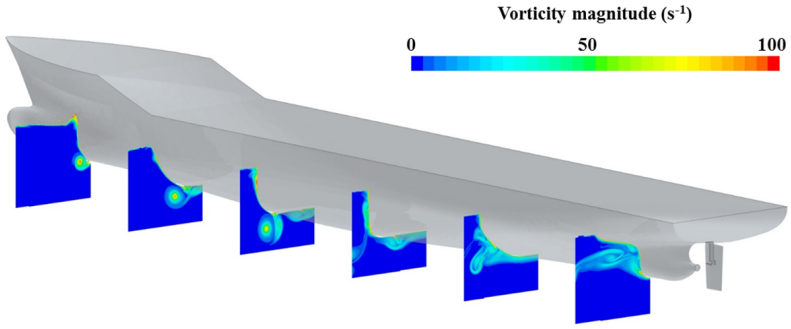

(**d**) drift angle of 12°

Figure 13. Vorticity magnitude in different static drift tests.

Figure 14 depicts the simulation results of lateral force using the RANS method and DES method. Two drift conditions are investigated, including drift angles of 6° and 12°. Subscripts of '*P*' and '*S*' in plots stand for the portside and starboard side, respectively. Disparities are mainly distributed at the portside, where incoming fluid originates. An abrupt variation of $F_{y,P}$ solved by the RANS method is visible around the center of the vessel in Figure 14a, with a maximum value and a minimum value. However, the distribution pattern obtained by the DES method, representing a smoother transition at the portside, does not match that of the RANS method. Concerning the starboard side, divergence can hardly be observed when the drift angle is 6°. When the drift angle increases to 12°, the variation tendency of $F_{y,S}$ calculated by DES is similar to that of the 6° static drift condition, showing distinct differentiation from the results of the RANS method. As illustrated in Table 8, the dimensionless sway force acting on the hull under the condition of β = 6°, solved by the DES method, is 2.412 × 10^{-2}. The corresponding relative error compared with experimental data is 3.17%. For the 12° static drift test, the value of Y' predicted by the DES method is 6.168 × 10^{-2}, which is close to the result achieved from the RANS method as shown in Table 7. The above analysis demonstrates the outperformance of the DES method in capturing details of vorticities, which is in accordance with the conclusion from predecessors' work [17]. For the sake of predicting hydrodynamic forces and moments, the utilization of the RANS model is preferable, taking efficiency and accuracy into account.

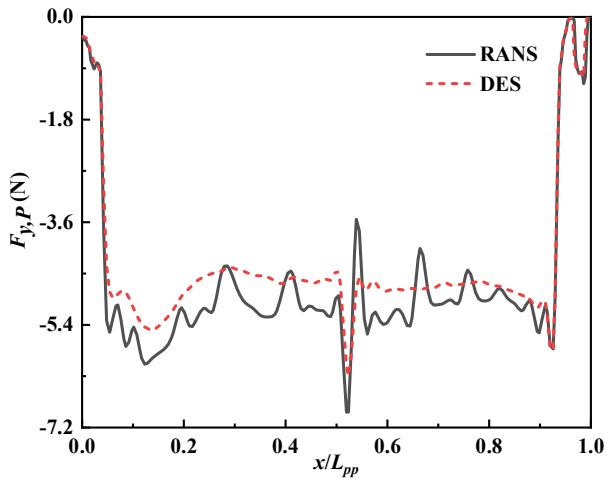

(**a**) portside at β = 6°

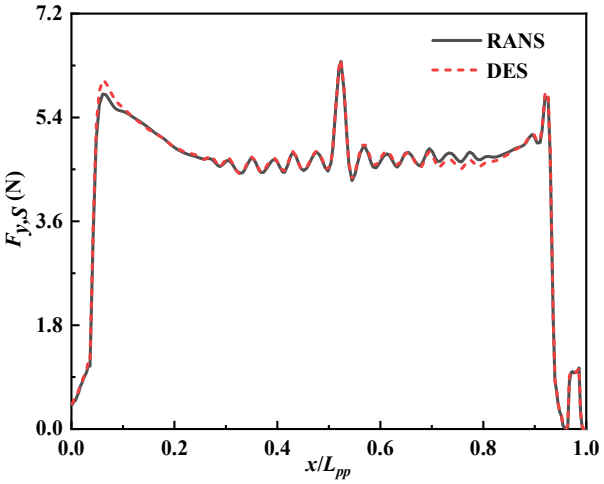

(**b**) starboard side at β = 6°

Figure 14. *Cont.*

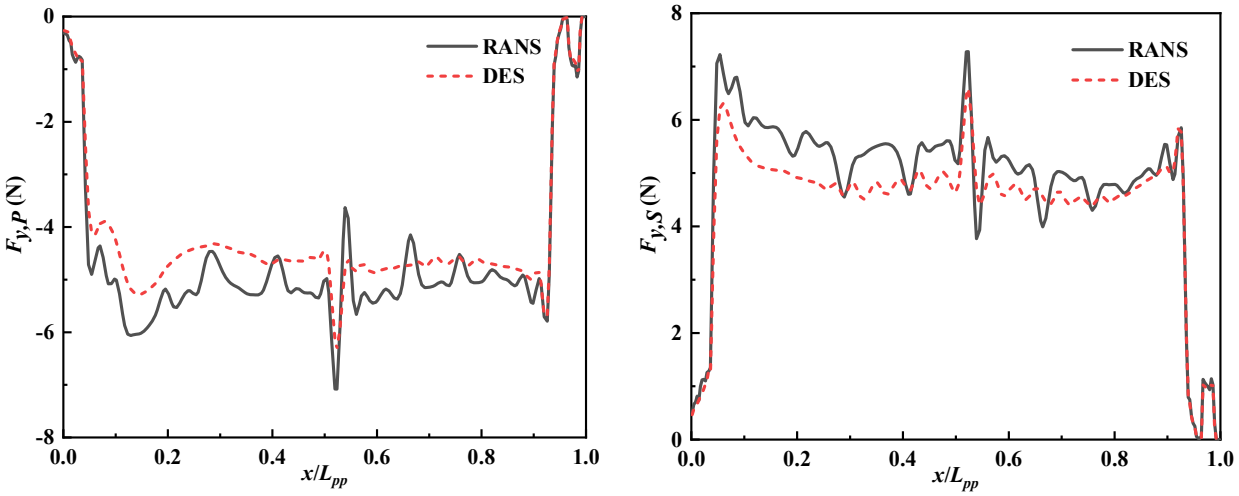

(**c**) portside at $\beta = 12°$ (**d**) starboard side at $\beta = 12°$

Figure 14. The comparison of lateral force through the RANS method and DES method.

Table 8. Validation of the DES model compared with experimental data provided by NMRI.

Drift Angle	Physical Quantity	Experimental Data ($\times 10^{-2}$)	Numerical Result ($\times 10^{-2}$)	Relative Error (%)
$\beta = 6°$	Y'	2.338	2.412	3.17
	N'	1.271	1.356	6.71
$\beta = 12°$	Y'	6.894	6.168	−10.53
	N'	2.455	2.744	12.99

4. Conclusions

A systematic analysis is conducted qualitatively and quantitatively to explore the roles of three influence factors in the computational study of the KCS. The aim of simulation determines the selection of the computational method. After the discussion of the oblique flow field in virtual static captive tests, some conclusions are addressed in the following:

Among influence factors of the grid size, turbulence model, and time step, grid size plays the most significant role in numerical simulation, followed by the turbulence model. According to the verification of numerical results, the relative error of the yaw moment is larger compared with longitudinal force and lateral force.

From the oblique flow field, the diversity between the lateral force at the portside and the starboard side along the longitudinal direction becomes more conspicuous with a larger drift angle, especially in the bow region.

The DES method has irreplaceable advantages in providing detailed information about vortex structures. Nevertheless, the utilization of the RANS model is preferable for the sake of predicting hydrodynamic forces and moments.

Author Contributions: Conceptualization, C.Y. and K.Z.; methodology, C.Y., K.Z. and Z.Z.; software, C.Y. and K.Z.; validation, J.C. and Z.Z.; formal analysis, C.Y. and K.Z.; investigation, C.Y., K.Z. and J.C.; resources, C.Y. and K.Z.; data curation, J.C. and Z.Z.; writing—original draft preparation, C.Y.; writing—review and editing, K.Z. and S.B.; supervision, K.Z. and J.C.; project administration, S.B.; funding acquisition, S.B. All authors have read and agreed to the published version of the manuscript.

Funding: This research was funded by the National Natural Science Foundation of China (Grant No. 52271336).

Institutional Review Board Statement: Not applicable.

Informed Consent Statement: Not applicable.

Data Availability Statement: The data that support the findings of this study are available within the article.

Conflicts of Interest: The authors declare no conflict of interest.

Nomenclature

B_{wl}	beam at waterline	m
C_B	block coefficient	
f	gravity	N
F_i	test statistic	
f_i	degree of freedom	
Fr	Froude number	
F_y	lateral force	N
GM	metacentric height	m
h	wave height	m
K_{ij}	average values at targeted levels	
L_{pp}	length between perpendiculars	m
MS_i	mean square	
N'	non-dimensional yaw moment	
P	pressure	Pa
S	wetted surface area	m^2
T	draught	m
R_j	extreme deviation	
S_i	sum of the standard deviation	
v_m	velocity of ship	m/s
u_i	x-coordinate components of velocity	m/s
u_j	y-coordinate components of velocity	m/s
X'	non-dimensional longitudinal force	
X_p	part of longitudinal force deriving from pressure	N
X_s	part of longitudinal force deriving from friction	N
Y'	non-dimensional lateral force	
$Y_{E,ij}{}^{(a)}$	relative error of the orthogonal experimental test with a serial number of a	
$Y_{N,ij}{}^{(a)}$	simulation result of the orthogonal experimental test with a serial number of a	
Y_p	part of longitudinal force deriving from pressure	N
Y_s	part of longitudinal force deriving from friction	N
$y+$	dimensionless wall distance	
Abbreviations		
CFD	Computational Fluid Dynamics	
DES	Detached Eddy Simulation	
DPM	Discretized Propeller Model	
GCI	Grid Convergence Index	
KCS	KRISO Container Ship	
OEM	Orthogonal Experimental Method	
OTT	Oblique Towing Test	
RANS	Reynolds Averaged Navier Stokes	
RSM	Reynolds Stress Model	
SV	Stern Vortex	
TKE	Turbulent Kinetic Energy	
WW-SDTV	Windward Sonar Dome Tip Vortex	
Greek symbols		
β	drift angle	°
ε	dissipation rate	m^3/s^2
κ	turbulent kinetic energy	J/kg
μ	viscosity	Pa·s
ρ	density	kg/m^3
ω	dissipation rate	m^3/s^2
∇	volume of displacement	m^3

Subscripts	
i	influence factor
j	level
m	phase id
P	values of the portside
S	values of the starboard side

References

1. He, Z.; Liu, C.; Chu, X.; Negenborn, R.R.; Wu, Q. Dynamic anti-collision A-star algorithm for multi-ship encounter situations. *Appl. Ocean Res.* **2022**, *118*, 102995. [CrossRef]
2. Balagopalan, A.; Tiwari, K.; Rameesha, T.; Krishnankutty, P. Manoeuvring prediction of a container ship using the numerical PMM test and experimental validation using the free running model test. *Ships Offshore Struct.* **2020**, *15*, 852–865. [CrossRef]
3. Zhang, S.; Liu, J.; Li, S.; Yasukawa, H.; Wu, Q. Impact of bow shapes on hydrodynamic derivatives due to drifting conditions. *Ocean Eng.* **2022**, *245*, 110347. [CrossRef]
4. Bhushan, S.; Yoon, H.; Stern, F. Large grid simulations of surface combatant flow at straight-ahead and static drift conditions. *Int. J. Comput. Fluid D* **2016**, *30*, 356–362. [CrossRef]
5. Yang, J.; Feng, D.K.; Liu, L.W.; Wang, X.Z.; Yao, C.B. Research on the performance of pumpjet propulsor of different scales. *J. Mar. Sci. Eng.* **2022**, *10*, 78. [CrossRef]
6. Yoon, H.; Simonsen, C.D.; Benedetti, L.; Longo, T.; Toda, Y.; Stern, F. Benchmark CFD validation data for surface combatant 5415 in PMM maneuvers—Part I: Force/moment/motion measurements. *Ocean Eng.* **2015**, *109*, 705–734. [CrossRef]
7. Carrica, P.M.; Fu, H.P.; Stern, F. Computations of self-propulsion free to sink and trim and of motions in head waves of the KRISO Container Ship (KCS) model. *Appl. Ocean Res.* **2011**, *33*, 309–320. [CrossRef]
8. Kim, D.; Tezdogan, T.; Incecik, A. A high-fidelity CFD-based model for the prediction of ship manoeuvrability in currents. *Ocean Eng.* **2022**, *256*, 111492. [CrossRef]
9. Wang, J.H.; Wan, D.C. CFD investigations of ship maneuvering in waves using naoe-FOAM-SJTU solver. *J. Mar. Sci. Appl.* **2018**, *17*, 443–458. [CrossRef]
10. Cura-Hochbaum, A. Virtual PMM tests for manoeuvring prediction. In Proceedings of the 26th ONR Symposium on Naval Hydrodynamics, Rome, Italy, 17–22 September 2006.
11. Huang, S.X.; Jiao, J.L.; Chen, C.H. Numerical prediction of ship motion and slamming load characteristics in cross wave. *J. Mar. Sci. Technol.* **2022**, *27*, 104–124. [CrossRef]
12. Sun, H.B.; Yang, S.Q.; Xu, Y.F.; Xiao, J.F. Prediction of the pitch and heave motions in regular waves of the DTMB 5415 ship using CFD and MMG. *J. Mar. Sci. Eng.* **2022**, *10*, 1358. [CrossRef]
13. Kim, I.; Kim, C.; Kim, S. Estimation of the manoeuvrability of the KVLCC2 in calm water using free running simulation based on CFD. *Int. J. Nav. Archit. Ocean Eng.* **2021**, *13*, 466–477. [CrossRef]
14. Jin, Y.T.; Yiew, L.J.; Zheng, Y.Y.; Magee, A.R.; Duffy, J.; Chai, S.H. Dynamic manoeuvres of KCS with CFD free-running computation and system-based modelling. *Ocean Eng.* **2021**, *241*, 110043. [CrossRef]
15. Zhang, W.; Liu, Y.D.; Chen, C.; He, Y.P.; Tang, Y.Y.; Sun, J.J. Research on the parametric rolling of the KCS container ship. *J. Mar. Sci. Technol.* **2023**, *28*, 675–688. [CrossRef]
16. Yu, J.W.; Feng, D.K.; Liu, L.W.; Yao, C.B.; Wang, X.Z. Assessments of propulsion models for free running surface ship turning circle simulations. *Ocean Eng.* **2022**, *250*, 110967. [CrossRef]
17. Hough, G.R.; Ordway, D.E. The generalized actuator disk. *Dev. Theor. Appl. Mech.* **1964**, *2*, 317–336.
18. Tokgoz, E. A CFD Study on the Propeller-Hull Interaction Flow in Waves Using Body-Force Distribution Model. Ph.D. Thesis, Osaka University, Osaka, Japan, 2015.
19. Feng, D.; Yu, J.; He, R.; Zhang, Z.; Wang, X. Improved body force propulsion model for ship propeller simulation. *Appl. Ocean Res.* **2020**, *104*, 102328. [CrossRef]
20. Simonsen, C.D.; Otzen, J.F.; Joncquez, S.; Stern, F. EFD and CFD for KCS heaving and pitching in regular head waves. *J. Mar. Sci. Technol.* **2013**, *18*, 435–459. [CrossRef]
21. Can, U.; Delen, C.; Bal, S. Effective wake estimation of KCS hull at full-scale by GEOSIM method based on CFD. *Ocean Eng.* **2020**, *218*, 108052. [CrossRef]
22. Kim, D.; Song, S.; Tezdogan, T. Free running CFD simulations to investigate ship manoeuvrability in waves. *Ocean Eng.* **2021**, *236*, 109567. [CrossRef]
23. Feng, D.K.; Ye, B.; Zhang, Z.G.; Wang, X.Z. Numerical simulation of the ship resistance of KCS in different water depths for model-scale and full-scale. *J. Mar. Sci. Eng.* **2020**, *8*, 745. [CrossRef]
24. Di Mascio, A.; Broglia, R.; Muscari, R. Numerical simulations of viscous flow around a fully appended hull with enforced motion. In Proceedings of the 9th Numerical Ship Hydrodynamics Conference, Ann Arbor, MI, USA, 5–8 August 2007.
25. Yuan, Z.M. Ship hydrodynamics in confined waterways. *J. Ship Res.* **2019**, *63*, 16–29. [CrossRef]
26. SIMMAN. Workshop on Verification and Validation of Ship Manoeuvring Simulation Methods. 2014. Available online: https://simman2014.dk (accessed on 8 December 2014).
27. Islam, I.; Soares, C.G. Uncertainty analysis in ship resistance prediction using OpenFOAM. *Ocean Eng.* **2019**, *191*, 105805. [CrossRef]

28. Visonneau, M.; Guilmineau, E.; Rubino, G. Local Flow around a surface combatant at various static drift conditions: The role played by turbulence closures. In Proceedings of the 33rd Symposium on Naval Hydrodynamics, Osaka, Japan, 18–23 October 2020.
29. Durbin, P.A. Some Recent Developments in Turbulence Closure Modeling. *Annu. Rev. Fluid Mech.* **2018**, *50*, 77–103. [CrossRef]
30. Zhang, Y.N.; Wang, X.Y.; Zhang, Y.N.; Liu, C.Q. Comparisons and analyses of vortex identification between Omega method and Q criterion. *J. Hydrodyn.* **2019**, *31*, 224–230. [CrossRef]